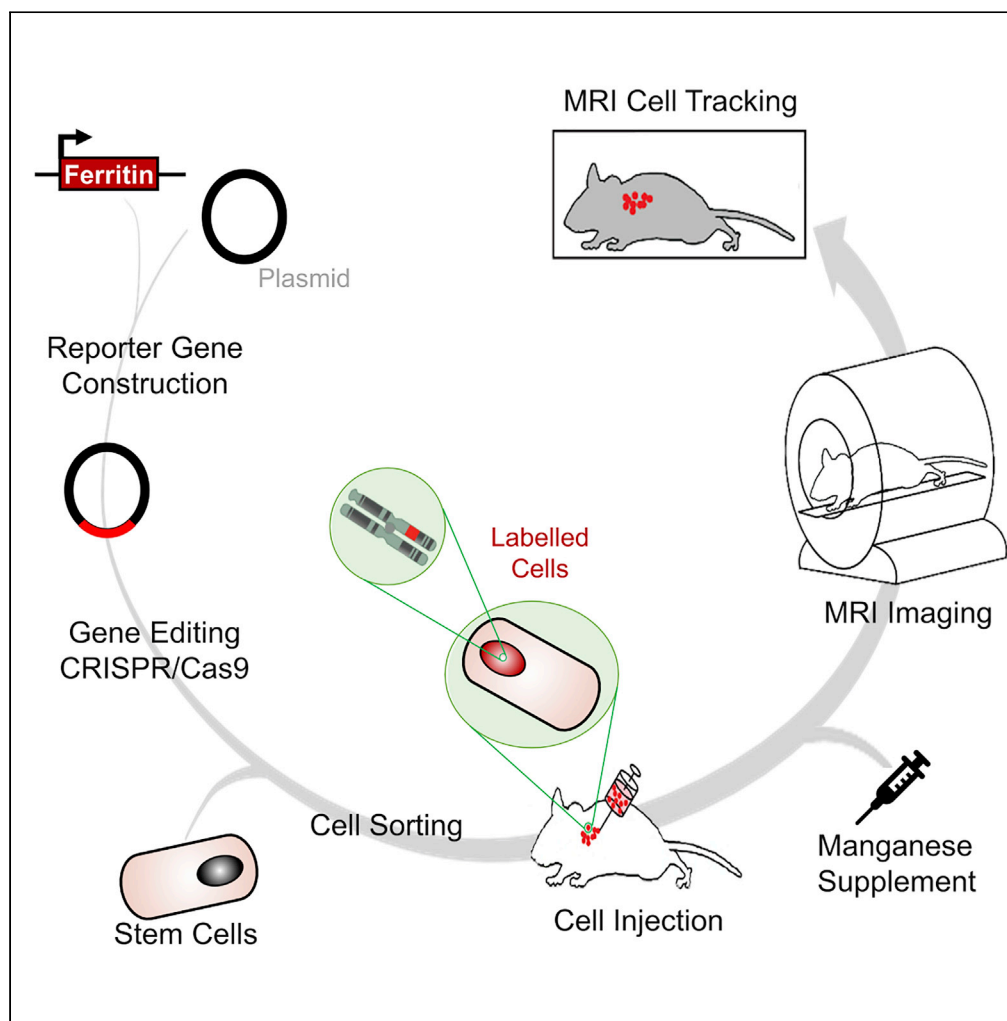## Article

Bright Ferritin—a Reporter Gene Platform for On-Demand, Longitudinal Cell Tracking on MRI

Daniel A. Szulc, Xavier A. Lee, Hai-Ying Mary Cheng, Hai-Ling Margaret Cheng

hailing.cheng@utoronto.ca

HIGHLIGHTS

First bright-ferritin MRI gene reporter platform for longitudinal cell tracking

In vivo assembly of manganese nanoparticles for bright MRI contrast

On-demand, sensitive, non-invasive *in vivo* deep imaging of proliferating cells

Article

Bright Ferritin—a Reporter Gene Platform for On-Demand, Longitudinal Cell Tracking on MRI

Daniel A. Szulc,[1,2] Xavier A. Lee,[2,3] Hai-Ying Mary Cheng,[4] and Hai-Ling Margaret Cheng[1,2,5,6,*]

SUMMARY

A major unresolved challenge in cell-based regenerative medicine is the absence of non-invasive technologies for tracking cell fate in deep tissue and with high spatial resolution over an extended interval. MRI is highly suited for this task, but current methods fail to provide longitudinal monitoring or high sensitivity, or both. In this study, we fill this technological gap with the first discovery and demonstration of *in vivo* cellular production of endogenous bright contrast via an MRI genetic reporter system that forms manganese-ferritin nanoparticles. We demonstrate this technology in human embryonic kidney cells genetically modified to stably overexpress ferritin and show that, in the presence of manganese, these cells produce far greater contrast than conventional ferritin overexpression with iron or manganese-permeable cells. In living mice, diffusely implanted bright-ferritin cells produce the highest and most sustained contrast in skeletal muscle. The bright-ferritin platform has potential for on-demand, longitudinal, and sensitive cell tracking *in vivo*.

INTRODUCTION

In vivo cell tracking is valuable across a multitude of applications ranging from stem cell therapy to studies of cancer metastasis. To visualize and distinguish the cells of interest, we must impart to them a differential contrast against background tissue. The simplest approach is to label the cells directly, prior to injection or implantation, with an image modality-specific contrast agent, such as iron oxides for magnetic resonance imaging (MRI) (Li et al., 2013) or ^{18}F-FDG for nuclear medicine imaging (Lang et al., 2013). This exogenous labeling approach, however, works well only for short-term studies and cannot attain the desired capability for monitoring over the long term. Multiple factors underlie this shortcoming, foremost of which are label dilution upon cell division, leakage of contrast agent from cells (Venter et al., 2018), and non-specific labeling of macrophages that take up contrast agents released from dying cells (Ma et al., 2015). Longitudinal cell tracking requires a method that provides *sustained* contrast *specific* to the *viable* cells of interest. To date, the most promising solution to longitudinal cell tracking *in vivo* is via reporter genes.

A variety of reporter genes have been proposed over the years for use with different imaging modalities. Of note are firefly luciferase for bioluminescence imaging (Bernau et al., 2014), herpes simplex virus 1 thymidine kinase for nuclear medicine (Koehne et al., 2003), and ferritin for MRI (Naumova et al., 2010). Among the modalities suitable for cell tracking, MRI is particularly attractive, because it uniquely affords flexible background tissue contrast, unlimited tissue penetration depth, absence of radiation, and superior spatial resolution compared with nuclear medicine and bioluminescence imaging (Pan et al., 2010). Ferritin, a polymeric iron storage protein, is the most widely used among MR reporters (Cohen et al., 2005; Iordanova and Ahrens, 2012), as other MR gene reporter systems are less accessible owing to very low sensitivity or the requirement for specialized coils tuned to different nuclei (Chen et al., 2011; Patrick et al., 2015). Despite the success achieved with ferritin for cell tracking, however, there remain a number of technical challenges. The change in MR relaxation time is frequently small and the resulting signal drop modest (Naumova et al., 2014; Vande Velde et al., 2011); very high levels of ferritin and/or iron are required to achieve the requisite detection sensitivity (Deans et al., 2006; Genove et al., 2005), and the onset of signal change is slow as iron requires days to accumulate (Iordanova et al., 2010). Sensitive and longitudinal cell tracking remains an unmet need.

In this work, we describe a "bright-ferritin" mechanism for sensitive, longitudinal cell tracking *in vivo*. This approach uses the cell's ferritin machinery to self-assemble manganese (Mn) nanoparticles, which confer a

[1]Institute of Biomedical Engineering, University of Toronto, 164 College Street, RS407, Toronto, ON M5S 3G9, Canada

[2]Ted Rogers Centre for Heart Research, Translational Biology & Engineering Program, University of Toronto, Toronto, ON M5G 1M1, Canada

[3]Department of Physiology, University of Toronto, Toronto, ON M5S 1A8, Canada

[4]Department of Biology, University of Toronto Mississauga, Mississauga, ON L5L 1C6, Canada

[5]The Edward S. Rogers Sr. Department of Electrical & Computer Engineering, University of Toronto, Toronto, ON M5S 3G4, Canada

[6]Lead Contact

*Correspondence:
hailing.cheng@utoronto.ca

https://doi.org/10.1016/j.isci.2020.101350

positive contrast on MRI. While previous work in the 1990s had shown the *in vitro* nucleation and growth of Mn particles in the cavity of extracted ferritin protein under harsh chemical conditions (Mackle et al., 1993; Meldrum et al., 1991, 1995), we report herein, for the first time, the *in vivo* self-assembly of endogenous Mn nanostructures. The bright contrast gleaned from Mn-ferritin nanoparticles can overcome many limitations associated with conventional negative contrast from ferritin overexpression. The main advantages are: (1) higher specificity, as negative contrast cannot be clearly distinguished from intrinsically dark sources (e.g., tissue/air interface, microbleeds); (2) higher sensitivity, especially in intrinsically dark background tissues (e.g., skeletal muscle); (3) accurate delineation of cell distribution (i.e., no "blooming" artifact); and (4) the potential for quantitation. Our comparison of bright-ferritin against conventional "dark-ferritin" cell imaging both *in vitro* and *in vivo* confirmed a substantially greater sensitivity of cell detection for the former. Bright-ferritin is also shown to rival the sensitivity derived from another positive-contrast reporter gene, the divalent metal transporter-1 (DMT-1), a membrane channel protein whose overexpression leads to increased transmembrane transport of free Mn ions (Bartelle et al., 2013). Our exploitation of the cell's machinery for endogenous production of bright-contrast Mn-ferritin nanoparticles presents a paradigm shift in the utilization of ferritin for on-demand, longitudinal, and sensitive *in vivo* cell tracking in cell-based therapeutics.

RESULTS

In Situ Manganese Encapsulation by Ferritin-Overexpressing Cells

To demonstrate the bright-ferritin technology, we chose to overexpress the human ferritin protein using a non-viral CRISPR-Cas9 system for targeted integration into the AAVS1 "safe-harbor" locus in human embryonic kidney (HEK293) cells (Figure 1A). Monoclonal cell lines selected for enhanced levels of ferritin expression demonstrated stable gene and protein levels relative to wild-type cells (Figure S1).

The bright-ferritin effect, as will be shown shortly, results from endogenous self-assembly of Mn-ferritin nanoparticles. To confirm this mechanism of intracellular particle formation, stable HEK cell lines overexpressing ferritin were supplemented with free Mn in culture prior to intracellular imaging with transmission electron microscopy (TEM) (Figure 1B). Whole-cell TEM sections of mutant cells revealed visibly distinct aggregates of nanoparticles accumulating in vesicles, which themselves reside in lysosome-like structures (Figure 1C), an observation consistent with previous reports of subcellular localization of ferritin nanoparticles (Sibille et al., 1989). In contrast, wild-type cells contained minimal nanoparticles with no visible aggregates (Figure S2A). Furthermore, cell lysates were collected and immuno-precipitated with ferritin monoclonal antibody to extract and purify the intracellular ferritin. TEM of the ferritin protein purified from mutant cells post-Mn incubation revealed electron-dense metallic particles with discrete mineral cores averaging 5.4 ± 0.3 nm in diameter (Figure 1D), similar in size to endogenous ferritin-iron nanocages measured by TEM (Farrant, 1954; Watabe and Hoshino, 1976). Ferritin extracts purified prior to Mn incubation, however, contained no electron-dense metallic nanoparticles (Figure S2B). To confirm the identity of the metallic core, elemental analysis for Mn was conducted on the purified ferritin particles via inductively coupled plasma atomic emission spectroscopy (ICP-AES). Ferritin-overexpressing cells had over twice the Mn-ferritin content (Figure 1E) *and* twice the ferritin protein expression levels (Figure 1F) relative to wild-type cells.

Cellular Expression of Ferritin Provides Efficient Bright Contrast on MRI

In vitro MRI reveals substantial contrast enhancement from stable ferritin-overexpressing cells that assemble Mn-ferritin nanoparticles intracellularly. Figure 2 illustrates live-cell imaging on a clinical 3T MR scanner. Ferritin-overexpressing and wild-type cells, both with and without Mn supplementation, were imaged in glass tubes using conventional T_1-weighted imaging to visualize bright contrast and T_1 mapping to quantify contrast-induced longitudinal relaxation effects (Figure 2A). At baseline, ferritin-overexpressing and wild-type cells displayed similar contrast levels. Upon Mn supplementation, ferritin-overexpressing cells exhibited a T_1 that was ~2.5-fold lower than that of wild-type cells (Figure 2B), thus rendering a higher signal on T_1-weighted scans. For this reason, we dub this MRI reporter gene complex bright-ferritin, a nomenclature we shall use hereon to describe the turning "on" of bright contrast via the cell's ferritin machinery.

We next assessed the sensitivity of the bright-ferritin system relative to that achieved via other MR reporter gene systems (we used CRISPR-Cas9 targeting for all reporters; see Figure S1). The contrast efficiency of bright-ferritin (Figure 2C) was compared with that of conventional ferritin with iron supplementation
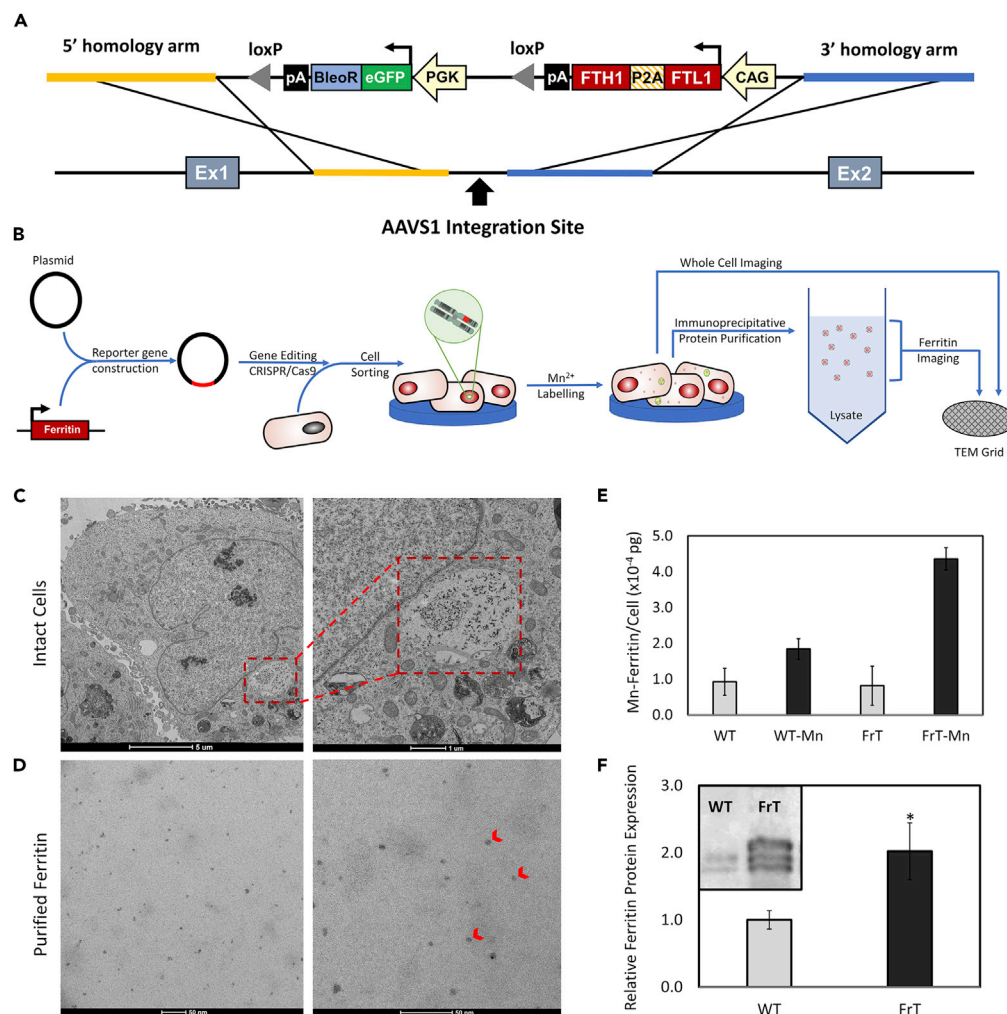
Figure 1. Engineering of Mammalian Bright-Ferritin Reporter Gene System

(A) Plasmid vector diagram for CRISPR-Cas9 gene editing for insertion of the human ferritin transgene at the AAVS1 locus.

(B–D) (B) Schematic of stable cell line generation and assay for intracellular nanoparticle formation. Representative TEM of (C) ferritin nanoparticle subcellular localization and (D) purified electron-dense ferritin nanoparticles (red arrowheads) extracted from ferritin-overexpressing cells supplemented with 0.2 mM $MnCl_2$ for 24 h.

(E) Cellular manganese content from purified ferritin nanoparticles in wild-type (WT) and ferritin-overexpressing (FrT) cells with or without Mn supplementation.

(F) Relative ferritin protein level normalized to α-tubulin in WT and FrT cells. Mn-incubated WT and FrT cells have different ferritin protein expression levels (*$p < 0.05$). Data in subfigures (E) and (F) are represented as mean $\pm$ SEM.

See also Figures S1 and S2.

(Figure 2D) and against free Mn transport via DMT-1 overexpression (Figure 2E). Illustrated in these graphs is the relationship between the change in relaxation rate ($R_1 = 1/T_1$ or $R_2 = 1/T_2$, depending on the MR reporter) and Mn or iron concentration. A steeper slope indicates a greater relaxivity associated with higher contrast efficiency. The bright-ferritin system had a high relaxivity of 17.7 $mM^{-1}s^{-1}$, exceeding those of engineered exogenous chemical agents and MR reporter gene gold standards (Alvares et al., 2017; Bartelle et al., 2013; Iordanova and Ahrens, 2012; Kalman et al., 2010; Sana et al., 2012). By comparison, ferritin overexpression with iron supplementation, the most widely used MR reporter system to date (Iordanova and Ahrens, 2012), had a very low relaxivity of 2.15 $mM^{-1}s^{-1}$. Even when a high dose of 0.9 mM iron was used to supplement ferritin-overexpressing cells, a modest 1.2-fold change in R_2 relative to wild-type was achieved. This low efficiency is the result of a lower ferritin protein overexpression from targeted CRISPR-Cas9 transfection, an approach we opted for over common non-targeted methods that entail undesired multiple insertions. To explore differences in signal generated from encapsulated Mn versus free
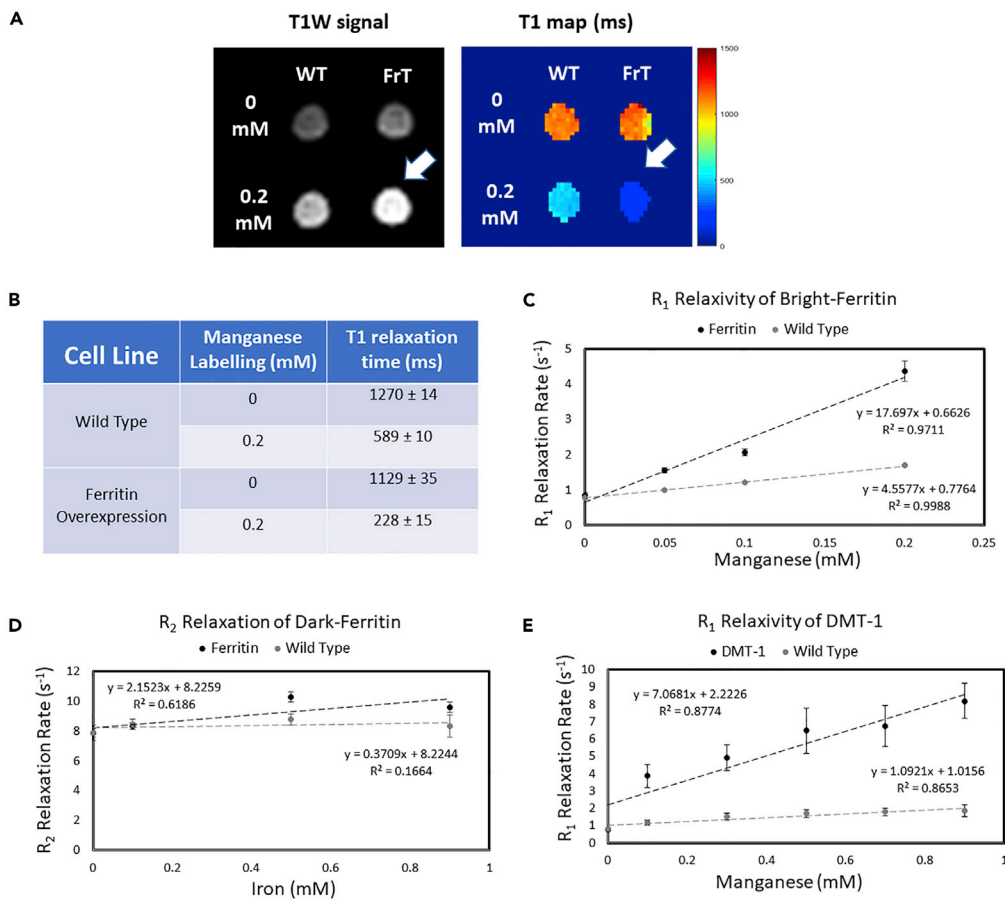
Figure 2. Bright-Contrast Efficiency *In Vitro* on MRI

(A) T_1-weighted spin echo image and T_1 map of wild-type (WT) and ferritin-overexpressing (FrT) cells incubated with 0.2 mM $MnCl_2$ for 24 h. Arrow indicates the bright-contrast cell pellet.

(B–E) (B) Tabulated mean T_1 value $\pm$ SD. The contrast efficiencies of all MR gene reporter systems are compared by measuring relaxation rate versus metal concentration; data are represented as mean $\pm$ SD (C–E).

Mn ions, we compared bright-ferritin against DMT-1. The DMT-1 system had a modest relaxivity of 7.1 mM^{-1}s^{-1}, most likely due to the challenge of cellular storage of free Mn. Clearly, bright-ferritin confers the highest contrast efficiency required for sensitive *in vivo* cell tracking.

Bright-Ferritin Is a Non-toxic MR Reporter Gene Complex

Absence of cellular toxicity is also very important in the setting of cell therapy. Not only must the cell-tracking technology be sensitive, but any modifications made to the therapeutic cells also cannot alter the cell's intended function to grow and replace tissue in the long-term. In our bright-ferritin platform, we introduced two modifications: gene editing for ferritin overexpression and Mn supplementation. To assess potential cytotoxicity associated with these modifications, we measured cell proliferation and metabolic activity for bright-ferritin and the other MR reporter systems at the optimal Mn or iron dose required for visible MR contrast. Cell viability and growth were assessed using a live/dead assay after dosing and expansion (Figure 3A). Cells were stained with a cell permeable/enzymatically activatable "green" fluorescent dye (Calcein AM) and a cell impermeable/DNA-binding "red" dye (EthD-1) to identify live and dead cells, respectively. Cell viability and growth were visually consistent at different time intervals between ferritin-overexpressing and wild-type cells. Minimal cell death and similar cell densities were observed for all reporter systems and treatment groups (Figure 3B). Cell metabolism assessed with WST-1 proliferation assay (Figure 3C), which quantitatively measures enzymatic activity in metabolically viable cells, showed no difference among the different reporter systems and treatment groups, indicating the absence of genomic stress or cytotoxicity from Mn supplementation.
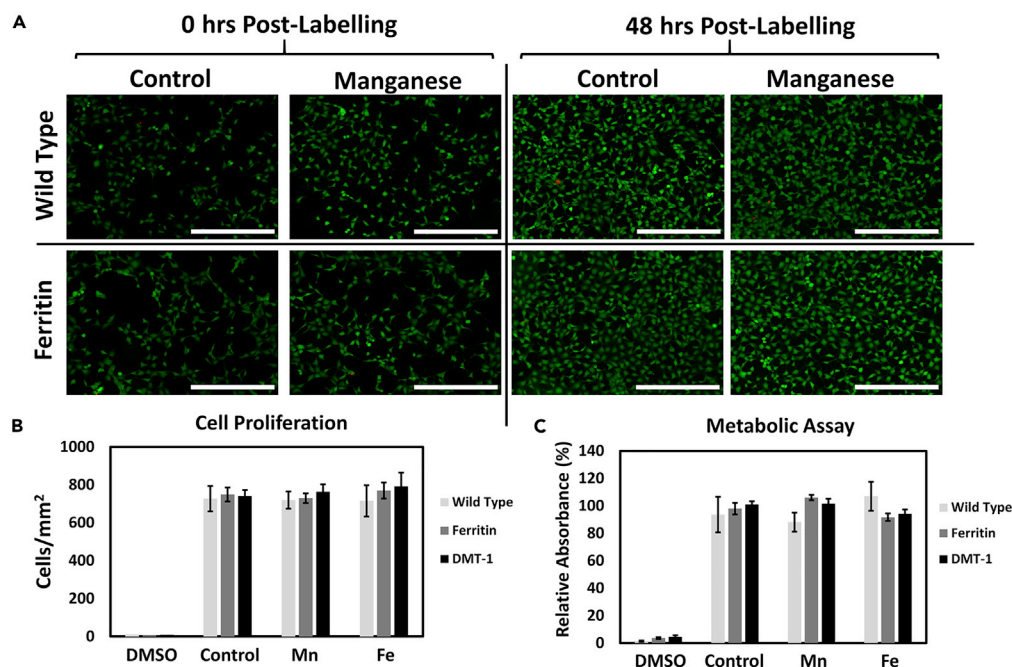
Figure 3. Biocompatibility of Genetic Reporter Systems

(A) Live (green)/dead (red) fluorescent assay at 0 and 48 h post Mn supplementation revealed minimal cell death and minimal impact on cell growth from ferritin overexpression and supplementation with 0.2 mM Mn for 24 h. Scale bar, 400 μm.

(B) Cell proliferation measured by cell density at 72 h after Mn supplementation (0.2 mM Mn for 24 h) or iron supplementation (0.9 mM Fe for 72 h).

(C) Metabolic (WST-1) assay for the same conditions as (B). Positive controls were treated with 5% dimethyl sulfoxide (DMSO). Negative controls were cultured in standard growth media with no additional supplementation. Data are represented as mean ± SEM.

Bright-Ferritin Is a Superior MR Reporter Gene for *In Vivo* Cell Tracking

Having validated the superior contrast efficiency of the bright-ferritin platform *in vitro*, our next challenge was to investigate its performance *in vivo*, where injected cells are likely to be diffuse and Mn exposure is poorly controlled at the site of cell injection owing to physiological variations. The performance of bright-ferritin, conventional dark-ferritin, and DMT-1 in NOD/SCID mice was evaluated longitudinally on a 3T MR scanner using quantitative MR relaxometry. Cells carrying the genetic reporters were injected into the muscle of one leg, and wild-type cells were injected in the contralateral leg. Histology confirmed the presence of viable cells distributed throughout the leg muscle (Figure S3). For the bright-ferritin and DMT-1 systems, free Mn was administered subcutaneously (s.c.) and allowed to accumulate for 24 h. For the conventional dark-ferritin system, in accordance with previous reports, no supplementation was given for the first 48 h to allow for endogenous iron buildup, after which animals were given daily oral doses of iron for five consecutive days.

Prior to contrast administration (day 1), none of the MR reporter systems presented differential contrast between the two legs (Figure 4A, top row). After Mn injection (day 2), bright contrast appeared in the leg containing bright-ferritin and DMT-1 cells relative to the contralateral leg containing wild-type cells. Notably, the signal enhancement produced by bright-ferritin was sustained visibly for up to 5 days, whereas the signal produced by DMT-1 had diminished by this time. To restore bright signal in the DMT-1 cells, a re-injection of Mn was required. In contrast to bright-ferritin and DMT-1, conventional dark-ferritin imaging produced no visible contrast relative to the contralateral leg. This was true during the first few days without iron supplementation (days 1 and 2) and even at later times with oral iron supplementation (days 5 and 7).

Quantitative MR relaxometry supported these visual findings. Both bright-ferritin and DMT-1 demonstrated a significant increase in R_1 after a single dose of Mn (Figure 4B). A maximum R_1 increase of 3.5-fold, 2.3-fold, and 1.5-fold relative to pre-contrast levels was achieved with the bright-ferritin, DMT-1,
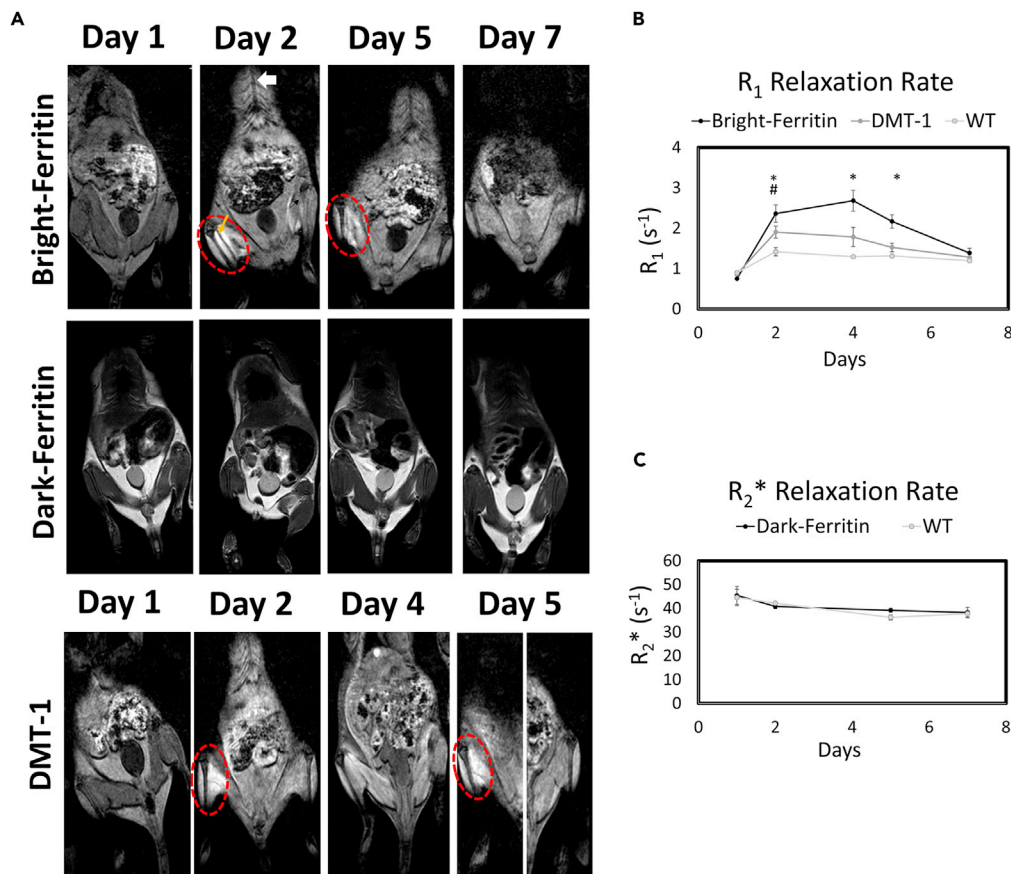
Figure 4. *In Vivo* MRI of HEK Cell Injections in Mice

(A) MRI of NOD/SCID mice injected with ferritin or DMT-1-overexpressing cells in the left leg and wild-type cells in the contralateral leg (site of cell injection indicated by yellow arrow). Subcutaneous $MnCl_2$ supplementation (administered subcutaneously at superior-inferior aspect indicated by white arrow) produced large signal enhancement in the leg containing bright-ferritin- (top row) and DMT-1- (bottom row) overexpressing cells. To recover signal loss in DMT-1 cells after 4 days, $MnCl_2$ was re-applied to turn "on" signal. Dark-ferritin cells (middle row) showed no contrast change, both without (day 1 and 2) and with iron supplement (day 5 and 7); oral iron supplementation was given daily after day 2. Quantitative relaxometry revealed (B) significant changes in R_1 in the bright-ferritin and DMT-1 legs relative to wild-type but (C) minimal difference in R_2^* on conventional dark-ferritin imaging. Difference in R_1 between bright-ferritin and DMT-1 is significant at all times (*$p < 0.05$); difference in R_1 between DMT-1 and wild-type is significant only at day 2 (#$p < 0.05$). Data are represented as mean $\pm$ SD.

and WT systems, respectively. Enhanced relaxation rates were higher and maintained longer in the bright-ferritin system than in DMT-1. Unsurprisingly, the dark-ferritin system exhibited no temporal changes in R_2^* (Figure 4C). Note that R_2^* is used here instead of R_1, because in the dark-ferritin system, contrast arises from susceptibility effects.

In addition to considering temporal contrast changes relative to pre-contrast levels, we also assessed changes in contrast ratios (i.e., ferritin: wild-type or DMT-1: wild-type), as this metric represents the "sensitivity" of the different MR reporter platforms in distinguishing the cells of interest against background tissue (Figure 5A). Bright-ferritin provided the greatest change in relative contrast, with a maximum change in relative R_1 of ~2.0. By comparison, DMT-1 had a maximum change in relative R_1 of 1.3 and conventional dark-ferritin had negligible changes in relative R_2^*. Based on the literature and observed results, we suggest in the following a potential mechanism for the bright-ferritin and DMT-1 systems (Figure 5B). In the DMT-1 system, free Mn is transported into the cell via DMT-1 and other endogenous pathways (Au et al., 2008). DMT-1 is an active proton-coupled metal ion symporter, which means it catalyzes the co-transport of H^+ protons and divalent metals (e.g., Mn^{2+}). At neutral pH, it symports one proton for every divalent metal cation and its import capabilities is enhanced by increasing the extracellular proton concentration
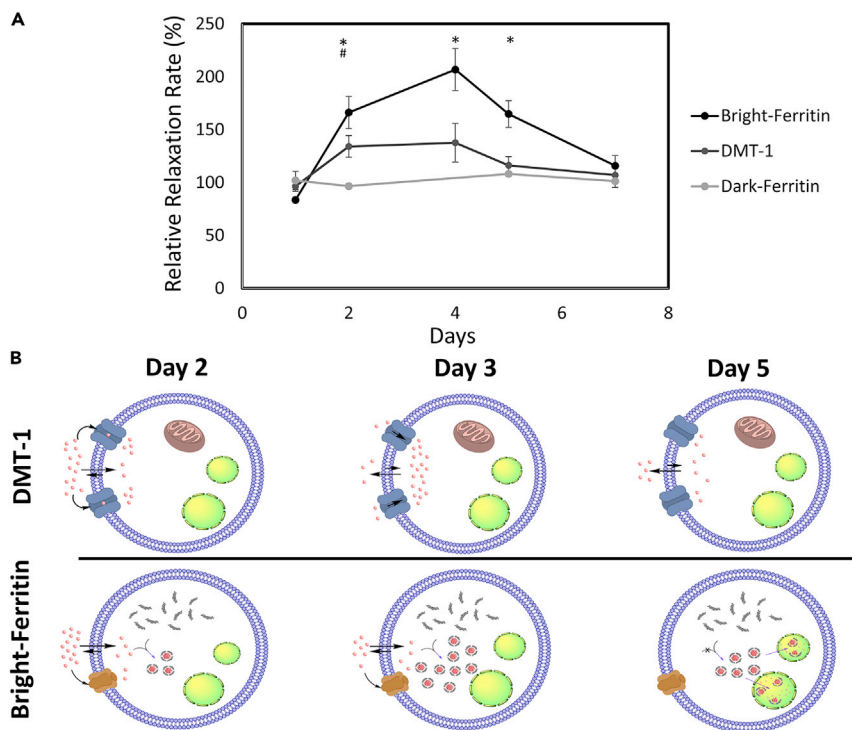
Figure 5. *In Vivo* Relative Contrast for Different MR Reporter Gene Systems

(A) Normalization of relaxation rates of the three gene reporter systems against wild-type HEK cells *in vivo*. Difference in relative R_1 between bright-ferritin and DMT-1 is significant from day 2 to 5 (*p < 0.01); difference in relative R_1 between DMT-1 and dark-ferritin is significant at day 2 (#p < 0.05). Data are represented as mean $\pm$ SD.

(B) Proposed mechanisms of contrast generation in the bright-ferritin and DMT-1 systems. Manganese transport and storage vary with time. Red dots represent Mn ions. Green organelles represent lysosome-like bodies.

(Gunshin et al., 1997; Moos and Morgan, 2000). As more Mn^{2+} and H^+ enter a cell, it is reasonable to expect the intracellular pH to decrease, thus reducing the proton gradient force that drives Mn uptake. The result is a plateau in Mn-induced signal, which we observed between days 2 and 4. As the extracellular concentration of Mn continues to drop, the rate of Mn uptake falls below that of Mn elimination, thus reducing intracellular Mn and bright contrast. It is important to emphasize that this postulation is difficult to validate completely, given our current understanding of the mechanisms underlying proton-coupled transporters is incomplete (Ehrnstorfer et al., 2017). It is also important to note that unlike most previous reports utilizing intravenous and intraperitoneal administration of Mn (Bartelle et al., 2013), we take advantage of s.c. injection for its slow release kinetics to achieve higher contrast and longer signal retention.

In the bright-ferritin system, Mn again enters the cell via endogenous mechanisms (Au et al., 2008). Once inside a cell, Mn does not remain in its ionic form but is sequestered by excess ferritin protein inside a mineral core. The sequestration slows the transition toward equilibrium (of free Mn), thus maintaining a gradient that drives Mn uptake into the cell over a prolonged interval. We postulate that Mn-ferritin particles do not remain indefinitely in the cytosol; rather, they are eventually engulfed in autophagosomes and the ferritin is ultimately degraded by lysosomal proteases. This hypothesis would be consistent with our observations on TEM, where we saw numerous dark puncta within a smaller vesicle found inside a lysosome-like structure. As the extracellular concentration of Mn continues to decrease, a point is reached where the rate of Mn-ferritin synthesis falls below the rate of ferritin turnover and Mn excretion. The result is a decline of intracellular Mn content and bright contrast.

DISCUSSION

We report here the first utilization of a cell's own machinery for *in vivo* cellular synthesis of endogenous Mn-ferritin nanoparticles to enable sensitive and non-invasive bright-contrast cell tracking over long intervals. This MRI platform, which we call bright-ferritin, seeks to attain the long-sought goal of

longitudinal cell tracking in regenerative medicine, and it does so via the use of reporter genes for endogenous contrast generation in viable cells. To compete with the sensitivity provided by short-lived exogenous cell labeling methods, the bright-ferritin system must break the low sensitivity ceiling that had hindered MR reporter gene systems. In this work, we proved *in vivo* and *in vitro* the superior sensitivity and contrast efficiency of bright-ferritin relative to other MR reporters, including conventional dark-contrast imaging using iron-ferritin particles and bright-contrast cell imaging using DMT-1 overexpression. Importantly, we achieved high detection sensitivity without introducing genomic stress and using low, non-toxic levels of exposure to Mn supplementation. The new bright-ferritin platform meets the key requirements for a practical cell-tracking technology in regenerative medicine: longitudinal monitoring capability, no ionizing radiation or radioactive tracers, unlimited depth penetration, high spatial resolution, high sensitivity to the viable cells of interest, high specificity to exclude non-targeted cells, and absence of cytotoxicity.

An important consideration with genetic modification is the potential for unintended off-target mutations and alteration of vital cell functions. We must limit not only the number of insertions but also the locations of insertions. It is for this reason that we adopted CRISPR-Cas9 to perform a single, targeted insertion at the "safe-harbor" AAVS1 locus. Although our approach minimizes the risk of deleterious effects, it also reduces the protein expression level, and, therefore, the amount of available contrast, compared with common non-targeted insertions that achieve very high overexpression (up to 60-fold) of MR genetic reporters (Bartelle et al., 2013; Genove et al., 2005; Iordanova et al., 2010; Thomas and Smart, 2005; Tiffen et al., 2010). This difference—single, targeted versus multiple, non-targeted insertions—may explain why we obtained negligible contrast with conventional dark-ferritin when many have reported modest contrast changes. The fact that our bright-ferritin system was able to furnish large contrast changes at low ferritin levels is exceedingly beneficial, as high protein overexpression commonly employed can create cellular stress and non-targeted systems are very unlikely to enter the clinical domain. These "safety" attributes of our bright-ferritin platform are essential attributes in any system intended for integration in the body for tissue regeneration.

The attainable sensitivity of a cell-tracking system can be determined only in an *in vivo* setting, where the diffusion and migration of injected cells against a background of non-uniform tissue, which are absent in a controlled *in vitro* setting, together with limited control over Mn distribution to the cell injection site, can substantially diminish the contrast achievable. Despite these *in vivo* challenges, our bright-ferritin system could readily identify and track diffuse cell populations over days in the mouse leg and with a high degree of detection sensitivity. It is equally important to emphasize that the capability for targeted imaging afforded by our system overcomes a longstanding limitation of exogenous nanoparticles and traditional cellular imaging methods (Tietjen et al., 2018). Our system now lays the foundation for enhanced non-invasive cell monitoring, with the ability to assess cell death in the early days post injection, cell migration throughout tissue over time, and continued cell growth from the original injected population. Furthermore, our use of bright contrast (as opposed to dark contrast with traditional ferritin) opens the door to cell tracking in inherently low-signal tissues such as skeletal and cardiac muscle (Naumova et al., 2010). Although not investigated fully in this work, the possibility exists with bright-contrast mechanisms for quantification of cell numbers. On this point, it is interesting to note the consistency we observed in ferritin protein overexpression (2-fold increase), cellular Mn-ferritin content (2.2-fold increase), *in vitro* change in R_1 (2.3-fold increase), and *in vivo* change in R_1 (2-fold increase). This high degree of correlation between ferritin overexpression, Mn content, and MR contrast changes strongly indicates a robust and controllable platform with quantitative cell-tracking capabilities.

One seemingly peculiar phenomenon is why, at low concentrations, Mn is able to provide a large change in contrast whereas iron cannot. The answer lies in the inherent difference by which Mn and iron nanoparticles alter MR relaxation rates underlying contrast changes. Iron nanoparticles, when aggregated at high concentrations, can effectively distort the local magnetic field, thus creating a change in the transverse relaxation rate R_2^* that produces dark signal. However, to effect a significant distortion of the local field, there must be an abundance of iron nanoparticles. With our low level of ferritin overexpression, we did not reach the particle concentration required for a measurable R_2^* effect. On the other hand, Mn nanoparticles produce contrast changes by altering the R_1 relaxation rate of the water protons with which the particles interact. High concentrations of Mn particles are not required for a large pool of water molecules to interact with the Mn ion, because water exchanges very rapidly at a rate of approximately one million times per second.

Another consideration on the topic of contrast efficiency is the impact of the environment on the effective relaxivity of Mn. We measured a longitudinal relaxivity of 17.7 mM^{-1}s^{-1} per Mn ion in our *in vitro* cell studies, which is over two times higher than an average of 6.2 mM^{-1}s^{-1} reported for Mn-loaded ferritin in solution without cells (Kalman et al., 2010). This difference is partly due to the rotational diffusion of the complex, which is expected to be slower inside a cell than it is in solution, thus accounting for slower tumbling and increased relaxivity. Furthermore, our measured relaxivity is representative of the entire cellular system, which includes not only ferritin-bound Mn but also free Mn in the cytosol and Mn ions bound to organelle membranes. This latter portion, which is ascribed to non-ferritin Mn, can be approximated by the effect measured in wild-type cells (Figure 2B). However, the precise proportion of bound versus free Mn cannot be derived from T_1 changes alone, because relaxation effects differ between free and bound Mn, as the free ion pool has a smaller effect from rotational diffusion but exchanges very rapidly with water.

There is also the question of what bright-contrast mechanism is best for a particular application. In this work, we characterized the performance of both bright-ferritin and DMT-1. Bright-ferritin produces contrast via the endogenous synthesis of Mn particles, whereas DMT-1 produces contrast via enhancing cellular uptake of free Mn ions. The choice of one over the other ultimately depends on whether a differential toxicity threshold exists between the two. For some cells, there may be no difference. For other cell types, there may be lower compatibility with one mechanism versus the other, because Mn in its ionic form affects cells differently compared with Mn stored in a particle. Neural cells, for example, which are highly sensitive to free ion concentrations, are unlikely to work well with DMT-1, given the vast literature evidence on Mn-related neural toxicity (Wennberg, 1994). The utility of bright-ferritin across a wide array of cell types remains to be explored.

The immediate next step is further pre-clinical investigation of the bright-ferritin technology in different cell therapy platforms. The relatively low cost of requisite materials means the method is easily and repeatedly accessible. Conceivably, any desired cell type can be tracked and against any background tissue, including low-signal tissues that previously failed to provide contrast differences relative to injected cells (Bernau et al., 2016; Pereira et al., 2015; Vande Velde et al., 2012; Vande Velde et al., 2011). More detailed longitudinal studies are needed in animal models to characterize the mechanism of particle elimination, test and retest the turning on of bright signal from the target cells, and uncover differences (if any) in tissue regeneration relative to wild-type cells. At a cellular level, mechanistic studies that provide precise characterization of relaxation effects will be valuable. Building on analogous studies in iron-ferritin systems (Herynek et al., 2000; Vymazal et al., 1996), these future investigations would involve cell systems in which the ferritin-bound Mn fraction is separated out; Mn binding location and loading factor within the nanocage would also be determined. Additionally, the influence of Mn in other cellular compartments such as the cytosol and organelles, whether bound or free, and their influence on relaxation, would be elucidated to provide system insight. Translation into the clinical domain, however, would require further technical and safety characterization and optimization. Rigorous genomic testing is required to ensure the cells are completely safe for injection. We may wish to tailor the mode of administering Mn supplement, such as localized delivery to the injection site or oral supplementation, thus providing an opportunity for further dose reduction. Although these questions remain to be answered, we do have insight on the answers to some questions. For example, our Mn-ferritin nanoparticles had standard core diameters. Particle size is an important parameter, because it dictates a particle's function, permeability, and uptake/degradation (Hoshyar et al., 2016; Theil et al., 2008). By maintaining the size of native ferritin, the particle has a high likelihood of behaving naturally like endogenous ferritin and undergoing similar routes of formation and degradation. Also, there is evidence from *in vitro* studies performed in solution that Mn can initially bind to ferritin with a stoichiometry of eight ions per molecule (Wardeska et al., 1986), and with specific binding to the ferroxidase center (Ardini et al., 2018); following this, a Mn oxyhydroxide (β-MnOOH) core is formed with various loading amounts from 500 to 4,000 Mn atoms per protein (Meldrum et al., 1991, 1995).

In conclusion, we report the first *in vivo* MRI cell tracking system that exploits ferritin in combination with manganese supplementation for the endogenous production of highly efficient bright contrast with greater sensitivity and retention than current MR reporters. This bright-ferritin system opens the door for accurate longitudinal monitoring of cell fate, available on demand, across a broad spectrum of applications in regenerative medicine.

Limitations of the Study

The generalized value of the bright-ferritin reporter system has not been investigated across a wide variety of cell types. Further studies are required to establish both sensitivity and safety across different cells and systems. Very long-term monitoring over months and years also was not included in this work and will be considered in future trials that are applications driven. Finally, detailed investigations into potential impact on many other important aspects of cell function need to be undertaken.

Resource Availability

Lead Contact

Further information and requests for resources and reagents should be directed to and will be fulfilled by the Lead Contact, Prof. Hai-Ling Cheng (hailing.cheng@utoronto.ca).

Materials Availability

There are restrictions to the availability of the reporter gene constructs and the genetically modified cell lines owing to a patent filed on the invention and materials pertaining to the work presented herein. The cells generated in this study will be made available on request, but we may require a payment and/or a completed Materials Transfer Agreement if there is potential for commercial application.

Data and Code Availability

There are restrictions to the availability of dataset owing to a patent filed on the invention, materials, and data pertaining to the work presented herein.

METHODS

All methods can be found in the accompanying Transparent Methods supplemental file.

SUPPLEMENTAL INFORMATION

Supplemental Information can be found online at https://doi.org/10.1016/j.isci.2020.101350.

AUTHOR CONTRIBUTIONS

H.-L.M.C. contributed to (1) overall direction, conceptualization, and design of study; (2) design of *in vitro* and *in vivo* MRI experiments; (3) design and implementation of MRI protocols; (4) development of software for analyzing quantitative MRI data; (5) *in vitro* and *in vivo* MRI; and (6) quantitative MRI analysis. H.-Y.M.C. contributed to (1) design and generation of targeting constructs and (2) PCR analysis. D.A.S. contributed to (1) conceptualization and design of study, (2) generation of stable cell lines, (3) western blot and densitometric analysis, (4) cellular Mn uptake studies, (5) design and execution of protein extraction and purification, (6) electron microscopy sample preparation and imaging, (7) analytical manganese content analysis, (8) toxicity assays and histology, (9) *in vitro* and *in vivo* MRI, and (10) statistical analysis of MRI data. X.A.L. contributed to (1) generation of stable cell lines, (2) western blot analysis, and (3) protein purification. All authors contributed to manuscript drafting and approved the final version.

DECLARATION OF INTERESTS

A provisional patent on the technology described herein was filed on April 2, 2020.

Cheng HLM, Szulc DA, Cheng HYM, "Ferritin for cellular tracking utilizing T1-weighted MRI," United Kingdom. 2004892.2. Filed 2020-04-02.

REFERENCES

Alvares, R.D.A., Szulc, D.A., and Cheng, H.M. (2017). A scale to measure MRI contrast agent sensitivity. Sci. Rep. 7, 15493.

Ardini, M., Howes, B.D., Fiorillo, A., Falvo, E., Sottini, S., Rovai, D., Lantieri, M., Ilari, A., Gatteschi, D., Spina, G., et al. (2018). Study of manganese binding to the ferroxidase centre of human H-type ferritin. J. Inorg. Biochem. 182, 103–112.

Au, C., Benedetto, A., and Aschner, M. (2008). Manganese transport in eukaryotes: the role of DMT1. Neurotoxicology 29, 569–576.

Bartelle, B.B., Szulc, K.U., Suero-Abreu, G.A., Rodriguez, J.J., and Turnbull, D.H. (2013). Divalent metal transporter, DMT1: a novel MRI reporter protein. Magn. Reson. Med. 70, 842–850.

Bernau, K., Lewis, C.M., Petelinsek, A.M., Benink, H.A., Zimprich, C.A., Meyerand, M.E., Suzuki, M., and Svendsen, C.N. (2014). In vivo tracking of human neural progenitor cells in the rat brain using bioluminescence imaging. J. Neurosci. Methods 228, 67–78.

Bernau, K., Lewis, C.M., Petelinsek, A.M., Reagan, M.S., Niles, D.J., Mattis, V.B., Meyerand, M.E., Suzuki, M., and Svendsen, C.N. (2016). In vivo tracking of human neural progenitor cells in the rat brain using magnetic resonance imaging is not enhanced by ferritin expression. Cell Transpl. 25, 575–592.

Chen, A.P., Hurd, R.E., Gu, Y.P., Wilson, D.M., and Cunningham, C.H. (2011). (13)C MR reporter probe system using dynamic nuclear polarization. NMR Biomed. 24, 514–520.

Cohen, B., Dafni, H., Meir, G., Harmelin, A., and Neeman, M. (2005). Ferritin as an endogenous MRI reporter for noninvasive imaging of gene expression in C6 glioma tumors. Neoplasia 7, 109–117.

Deans, A.E., Wadghiri, Y.Z., Bernas, L.M., Yu, X., Rutt, R.K., and Turnbull, D.H. (2006). Cellular MRI contrast via coexpression of transferrin receptor and ferritin. Magn. Reson. Med. 56, 51–59.

Ehrnstorfer, I.A., Manatschal, C., Arnold, F.M., Laederach, J., and Dutzler, R. (2017). Structural and mechanistic basis of proton-coupled metal ion transport in the SLC11/NRAMP family. Nat. Commun. 8, 14033.

Farrant, J.L. (1954). An electron microscopic study of ferritin. Biochim. Biophys. Acta 13, 569–576.

Genove, G., DeMarco, U., Xu, H., Goins, W.F., and Ahrens, E.T. (2005). A new transgene reporter for in vivo magnetic resonance imaging. Nat. Med. 11, 450–454.

Gunshin, H., Mackenzie, B., Berger, U.V., Gunshin, Y., Romero, M.F., Boron, W.F., Nussberger, S., Gollan, J.L., and Hediger, M.A. (1997). Cloning and characterization of a mammalian proton-coupled metal-ion transporter. Nature 388, 482–488.

Herynek, V., Bulte, J.W., Douglas, T., and Brooks, R.A. (2000). Dynamic relaxometry: application to iron uptake by ferritin. J. Biol. Inorg. Chem. 5, 51–56.

Hoshyar, N., Gray, S., Han, H., and Bao, G. (2016). The effect of nanoparticle size on in vivo pharmacokinetics and cellular interaction. Nanomedicine (Lond) 11, 673–692.

Iordanova, B., and Ahrens, E.T. (2012). In vivo magnetic resonance imaging of ferritin-based reporter visualizes native neuroblast migration. Neuroimage 59, 1004–1012.

Iordanova, B., Robison, C.S., and Ahrens, E.T. (2010). Design and characterization of a chimeric ferritin with enhanced iron loading and transverse nmr relaxation rate. J. Biol. Inorg. Chem. 15, 957–965.

Kalman, F.K., Geninatti-Crich, S., and Aime, S. (2010). Reduction/dissolution of a beta-MnOOH nanophase in the ferritin cavity to yield a highly sensitive, biologically compatible magnetic resonance imaging agent. Angew. Chem. Int. Ed. 49, 612–615.

Koehne, G., Doubrovin, M., Doubrovina, E., Zanzonico, P., Gallardo, H.F., Ivanova, A., Balatoni, J., Teruya-Feldstein, J., Heller, G., May, C., et al. (2003). Serial in vivo imaging of the targeted migration of human HSV-TK-transduced antigen-specific lymphocytes. Nat. Biotechnol. 21, 405–413.

Lang, C., Lehner, S., Todica, A., Boening, G., Franz, W.M., Bartenstein, P., Hacker, M., and David, R. (2013). Positron emission tomography based in-vivo imaging of early phase stem cell retention after intramyocardial delivery in the mouse model. Eur. J. Nucl. Med. Mol. Imaging 40, 1730–1738.

Li, L., Jiang, W., Luo, K., Song, H., Lan, F., Wu, Y., and Gu, Z. (2013). Superparamagnetic iron oxide nanoparticles as MRI contrast agents for non-invasive stem cell labeling and tracking. Theranostics 3, 595–615.

Ma, N., Cheng, H., Lu, M., Liu, Q., Chen, X., Yin, G., Zhu, H., Zhang, L., Meng, X., Tang, Y., et al. (2015). Magnetic resonance imaging with superparamagnetic iron oxide fails to track the long-term fate of mesenchymal stem cells transplanted into heart. Sci. Rep. 5, 9058.

Mackle, P., Charnock, J.M., Garner, C.D., Meldrum, F.C., and Mann, S. (1993). Characterization of the manganese core of reconstituted ferritin by x-ray absorption spectroscopy. J. Am. Chem. Soc. 115, 8471–8472.

Meldrum, F.C., Douglas, T., Levi, S., Arosio, P., and Mann, S. (1995). Reconstitution of manganese oxide cores in horse spleen and recombinant ferritins. J. Inorg. Biochem. 58, 59–68.

Meldrum, F.C., Wade, V.J., Nimmo, D.L., Heywood, B.R., and Mann, S. (1991). Synthesis of inorganic nanophase materials in supramolecular protein cages. Nature 349, 684–687.

Moos, T., and Morgan, E.H. (2000). Transferrin and transferrin receptor function in brain barrier systems. Cell Mol. Neurobiol. 20, 77–95.

Naumova, A.V., Balu, N., Yarnykh, V.L., Reinecke, H., Murry, C.E., and Yuan, C. (2014). Magnetic resonance imaging tracking of graft survival in the infarcted heart: iron oxide particles versus ferritin overexpression approach. J. Cardiovasc. Pharmacol. Ther. 19, 358–367.

Naumova, A.V., Reinecke, H., Yarnykh, V., Deem, J., Yuan, C., and Murry, C.E. (2010). Ferritin overexpression for noninvasive magnetic resonance imaging-based tracking of stem cells transplanted into the heart. Mol. Imaging 9, 201–210.

Pan, D., Caruthers, S.D., Chen, J., Winter, P.M., SenPan, A., Schmieder, A.H., Wickline, S.A., and Lanza, G.M. (2010). Nanomedicine strategies for molecular targets with MRI and optical imaging. Future Med. Chem. 2, 471–490.

Patrick, P.S., Kettunen, M.I., Tee, S.S., Rodrigues, T.B., Serrao, E., Timm, K.N., McGuire, S., and Brindle, K.M. (2015). Detection of transgene expression using hyperpolarized 13C urea and diffusion-weighted magnetic resonance spectroscopy. Magn. Reson. Med. 73, 1401–1406.

Pereira, S.M., Moss, D., Williams, S.R., Murray, P., and Taylor, A. (2015). Overexpression of the MRI reporter genes ferritin and transferrin receptor affect iron homeostasis and produce limited contrast in mesenchymal stem cells. Int. J. Mol. Sci. 16, 15481–15496.

Sana, B., Poh, C.L., and Lim, S. (2012). A manganese-ferritin nanocomposite as an ultrasensitive T2 contrast agent. Chem. Commun. 48, 862–864.

Sibille, J.C., Ciriolo, M., Kondo, H., Crichton, R.R., and Aisen, P. (1989). Subcellular localization of ferritin and iron taken up by rat hepatocytes. Biochem. J. 262, 685–688.

Theil, E.C., Liu, X.S., and Tosha, T. (2008). Gated pores in the ferritin protein nanocage. Inorg. Chim Acta 361, 868–874.

Thomas, P., and Smart, T.G. (2005). HEK293 cell line: a vehicle for the expression of recombinant proteins. J. Pharmacol. Toxicol. Methods 51, 187–200.

Tietjen, G.T., Bracaglia, L.G., Saltzman, W.M., and Pober, J.S. (2018). Focus on fundamental: achieving effective nanoparticle targeting. Trends Mol. Med. 24, P598–P606.

Tiffen, J.C., Bailey, C.G., Ng, C., Rasko, J.E., and Holst, J. (2010). Luciferase expression and bioluminescence does not affect tumor cell growth in vitro or in vivo. Mol. Cancer 9, 299.

Vande Velde, G., Raman Rangarajan, J., Vreys, R., Guglielmetti, C., Dresselaers, T., Verhoye, M., Van der Linden, A., Debyser, Z., Baekelandt, V., Maes, F., et al. (2012). Quantitative evaluation of MRI-based tracking of ferritin-labeled endogenous neural stem cell progeny in rodent brain. Neuroimage 62, 367–380.

Vande Velde, G., Rangarajan, J.R., Toelen, J., Dresselaers, T., Ibrahimi, A., Krylychkina, O.,

Vreys, R., Van der Linden, A., Maes, F., Debyser, Z., et al. (2011). Evaluation of the specificity and sensitivity of ferritin as an MRI reporter gene in the mouse brain using lentiviral and adeno-associated viral vectors. Gene Ther. 18, 594–605.

Venter, A., Szulc, D.A., Loai, S., Ganesh, T., Haedicke, I.E., and Cheng, H.L. (2018). A manganese porphyrin-based T1 contrast agent for cellular MR imaging of human embryonic stem cells. Sci. Rep. 8, 12129.

Vymazal, J., Zak, O., Bulte, J.W., Aisen, P., and Brooks, R.A. (1996). T1 and T2 of ferritin solutions:

effect of loading factor. Magn. Reson. Med. 36, 61–65.

Wardeska, J.G., Viglione, B., and Chasteen, N.D. (1986). Metal ion complexes of apoferritin. Evidence for initial binding in the hydrophilic channels. J. Biol. Chem. 261, 6677–6683.

Watabe, T., and Hoshino, T. (1976). Observation of individual ferritin particles by means of scanning electron microscope. J. Electron Microsc. (Tokyo) 25, 31–33.

Wennberg, A. (1994). Neurotoxic effects of selected metals. Scand. J. Work Environ. Health 20, 65–71.

Supplemental Information

Bright Ferritin—a Reporter Gene Platform

for On-Demand, Longitudinal Cell Tracking on MRI

Daniel A. Szulc, Xavier A. Lee, Hai-Ying Mary Cheng, and Hai-Ling Margaret Cheng
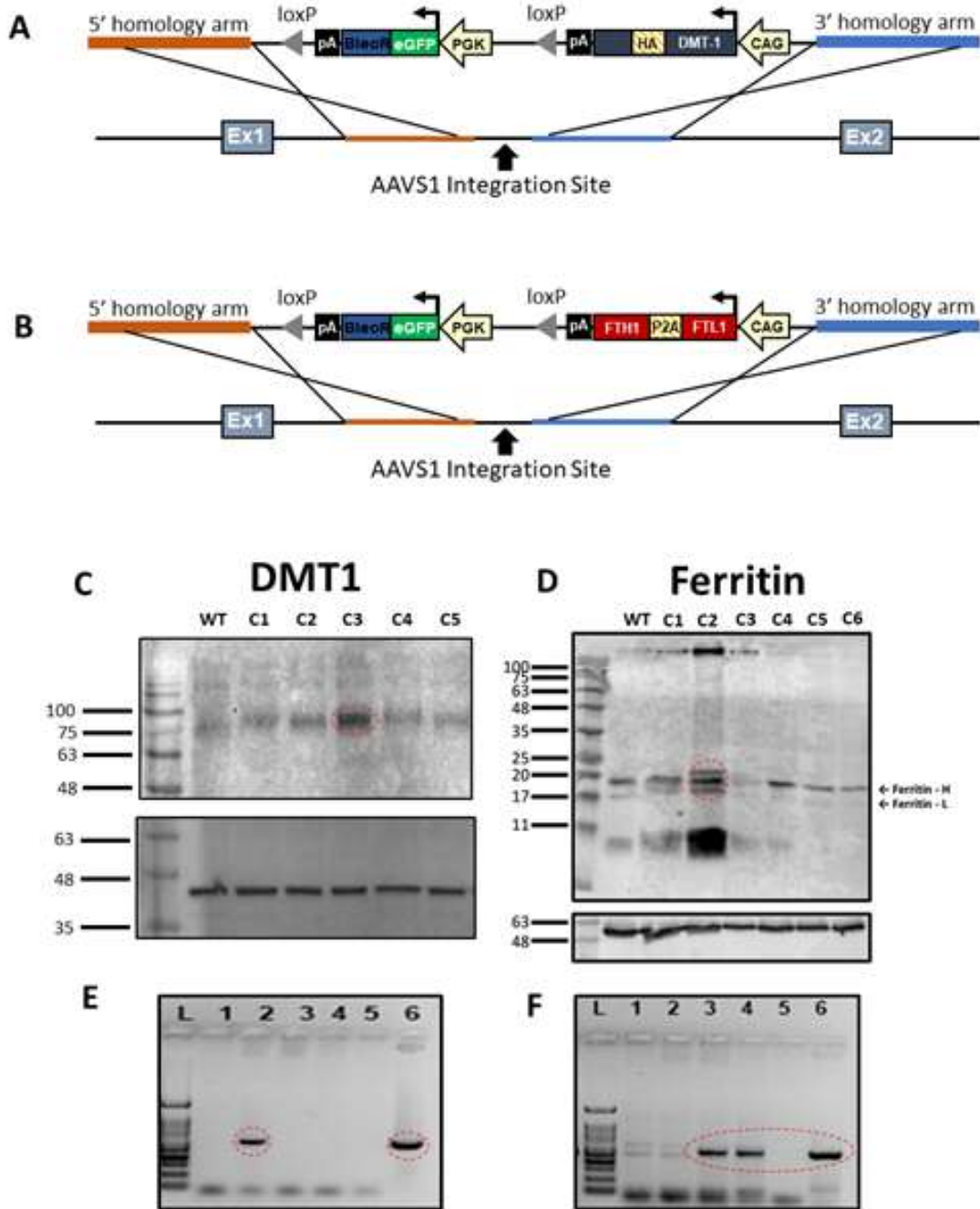
SUPPLEMENTAL FIGURES

Fig. S1: Western blots and PCR of stably transfected cells. Related to Fig. 1. Plasmid vector diagrams for CRISPR/Cas9 gene editing for insertion of **(A)** the DMT-1 transgene and **(B)** the human ferritin transgene at the AAVS1 locus. Western blots for cells overexpressing **(C)** DMT-1 protein and **(D)** ferritin protein. Directly below are the α-tubulin blots for loading control. PCR gels demonstrated enhanced PCR product and overexpression of the **(E)** DMT-1 gene and the **(F)** ferritin gene of transfected cells in comparison with the original DNA vector. Lanes in the PCR gels are as follows: L: ladder, 1: wild type cells, 2: DMT-1-overexpressing cells, 3: ferritin-overexpressing cells, 4: repeat ferritin-overexpressing cells, 5: water, 6: vector.
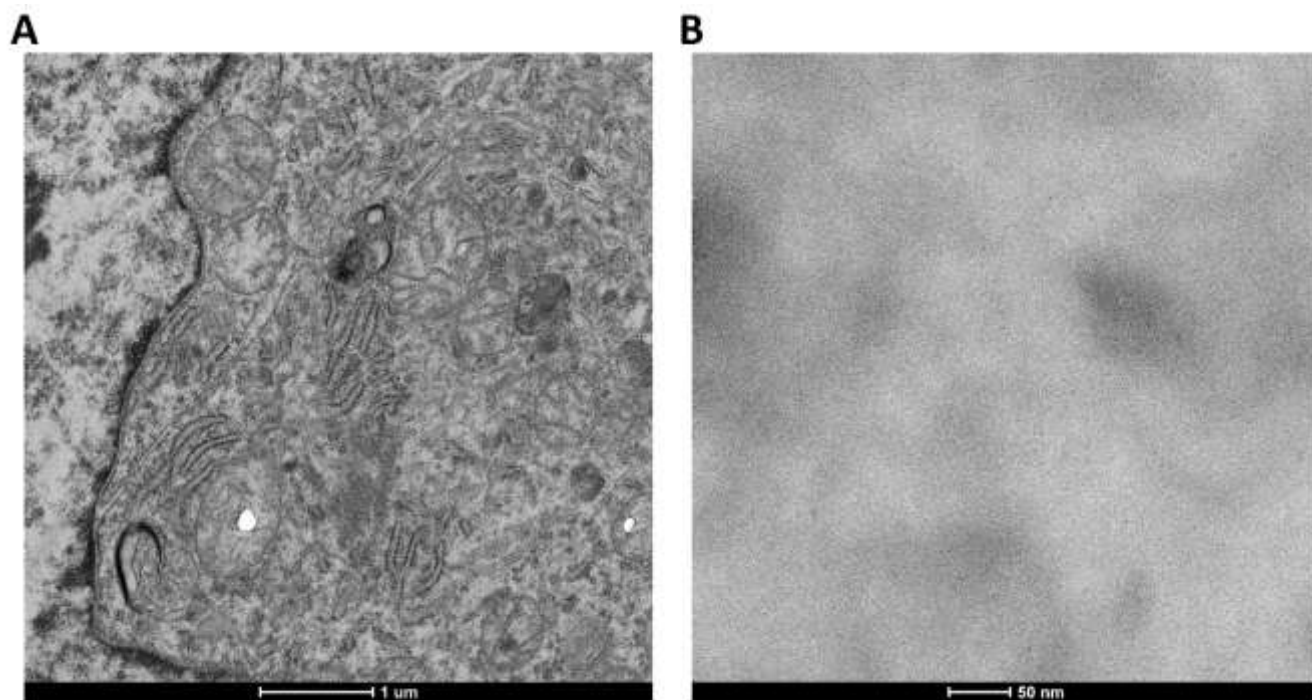
Fig. S2: Control Transmission Electron Micrographs (TEM). Related to Fig. 1. TEM of wild type cells **(A)** after incubation with 0.2 mM for 24 hours; no distinguishable nanoparticle aggregates are visible. TEM of purified ferritin nanoparticles **(B)** from ferritin-overexpressing cells before incubation with $MnCl_2$; electron-dense metallic particles are absent.
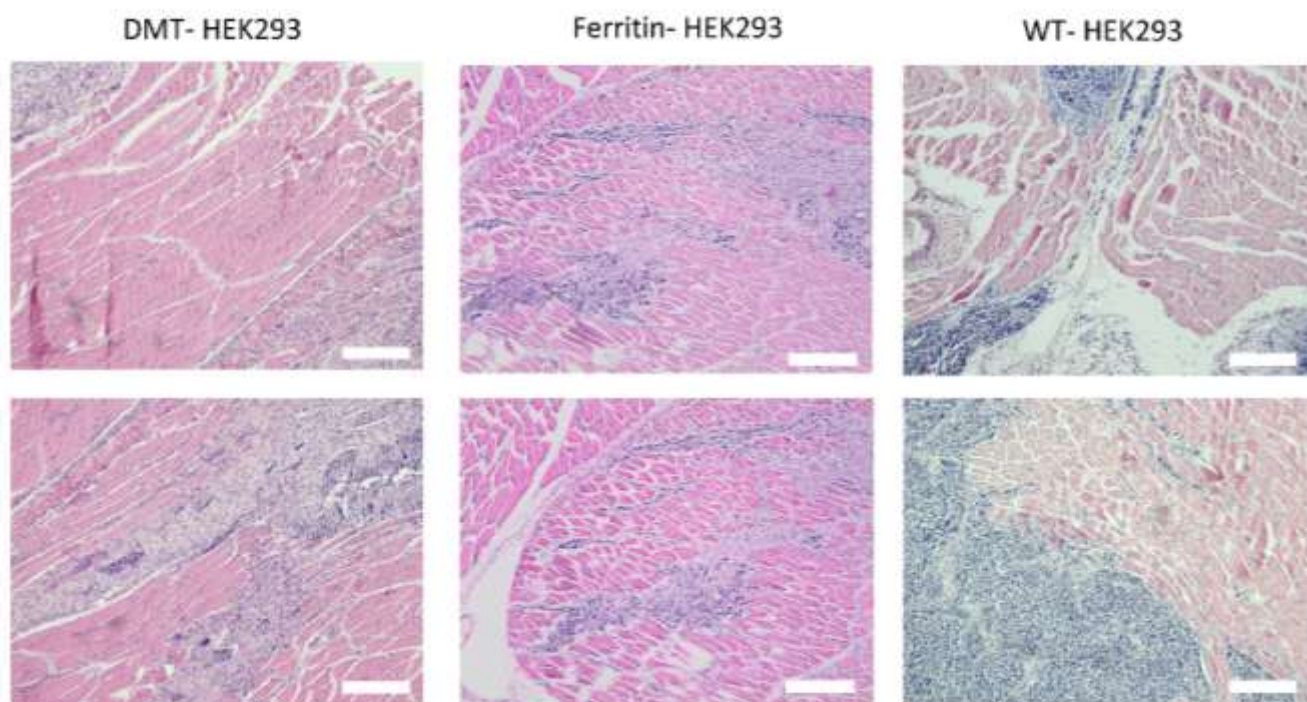

Fig. S3: Histology of cell injection sites in NOD/SCID mice on Day 7. Related to Fig. 4. Representative H&E staining of the inner leg muscle demonstrates the diffuse spread of injected HEK cells throughout the muscle. Scale bar = 50 um.

TRANSPARENT MATERIALS

Experimental design

In designing our MR reporter gene system, we sought to adhere to design criteria that would maximize the potential of our system for future translational work. With this in mind, we introduced our ferritin transgene using non-viral CRISPR technology for a single, targeted insertion at the "safe-harbor" locus. Once stable integration was attained, the next task was to optimize in vitro the labeling conditions (i.e. with metal ion supplementation) that would confer sensitivity of detection at the lowest possible dose. This, again, is consistent with our general philosophy of using the lowest overexpression, dosing, etc. necessary to achieve sensitivity of cell detection. In-vivo testing in immune-compromised mice was undertaken to demonstrate the practicality of the bright-ferritin system. Finally, extensive validation experiments were designed and undertaken to provide a biophysical understanding of how "bright-ferritin" contrast arises in cells.

DNA cloning, amplification, and purification

Gene synthesis of human ferritin heavy chain 1 (FTH1) and human ferritin light chain 1 (FTL1), codon-optimized for expression in human cells, was conducted by Genscript (Piscataway, NJ). The FTL1 gene fragment was subcloned into the pcDNA3.1(+)-P2A plasmid, upstream of and in-frame with the sequence for the P2A self-cleaving peptide. The Kozak sequence GCCACC was introduced before the start codon of FTL1 to promote protein expression. The FTH1 gene fragment was cloned downstream of the P2A sequence. The FTL1-P2A-FTH1 transgene sequence was then cloned downstream of the CAG promoter in a pzDonor plasmid. The final construct, pzDONOR-CAG-FTL1-P2A-FTH1-PGK-eGFP-BleoR, expresses FTL1-P2A-FTH1 under the control of the CAG promoter and the fusion of eGFP and the bleomycin resistance gene under the control of the PGK promoter (Fig. 1A).

Gene synthesis of mouse DMT-1 carrying an internal HA tag (Lam-Yuk-Tseung and Gros, 2006), codon-optimized for expression in human and mouse cells, was likewise carried out by Genscript. Kozak

and Shine Dalgarno sequences were added to increase the efficiency of translational initiation. The DMT-1 transgene was first subcloned into the pcDNA6/V5-His A plasmid and then cloned into the pzDonor plasmid to generate the final construct, pzDONOR-CAG-DMT-1-PGK-eGFP-BleoR (Fig. S1A).

For propagation of plasmids, DH5α *E. coli* cells were transformed and grown in Lysogeny Broth (LB) media supplemented with antibiotic. Plasmids were purified using Qiagen HiSpeed Plasmid Maxi kits (#12662). DNA concentration and purity were assessed quantitatively by UV absorbance at 260 and 280 nm using the NanoDrop™ 2000 UV Spectrometer (Thermo Scientific). Plasmids were verified by sequencing as well as restriction digestion analysis.

Stable cell line generation

All cell lines were generated with a non-viral CRISPR/Cas9 system for targeted integration into the AAVS1 safe-harbor locus. HEK293 cells were cultured in Dulbecco's minimal essential medium (DMEM) with 10% fetal bovine serum (FBS) and 1% penicillin/streptomycin (P/S). Cells were co-transfected with the AAVS1-T2-CRIPR vector (Addgene, #7283) along with either pzDONOR-CAG-FTL1-P2A-FTH1-PGK-eGFP-BleoR or pzDONOR-CAG-DMT-1-PGK-eGFP-BleoR constructs, resulting in CRISPR/Cas9 targeting of the reporter transgenes to the AAVS1 locus in human cells. Cells were transfected using a 3:1 ratio of polyethyleneimine (PEI) to vector DNA for 24 hours. Cells were then sorted for eGFP expression with a BD FACSAria II flow cytometer before expansion of single colonies to produce monoclonal cell lines. Clones were screened by polymerase chain reaction (PCR) to confirm integration of the reporter transgene into the genomic DNA and by immunoblotting to confirm transgene protein overexpression (Lee et al., 2020). Only those clones that exhibited the highest level of overexpression of DMT-1 or ferritin relative to wild type were selected for further tests.

Polymerase chain reaction (PCR)

Genomic DNA was extracted from select clones and analyzed by PCR for the presence of the correct transgene. To detect the presence of the DMT-1 transgene, forward and reverse primers recognizing HA

and DMT-1, respectively, were used in the PCR amplification reaction (HA-fwd:5'-CCCTATGACGTGCCTGATTACGC-3'; DMT-1-rev: 5'-CATCCCAGGTAGAACACGAAGGTC-3'). To detect the presence of the ferritin transgene, forward and reverse primers recognizing P2A and FTH1, respectively, were used (P2A-fwd: 5'-GGAGCTACTAACTTCAGCCTGCTG-3'; FTH1-rev: 5'-CTTCCGCAGATTGGTCACGTGATC-3'). Samples were electrophoresed on agarose gels and imaged with a Bio-Rad Gel Doc XR+. The pzDONOR-CAG-FTL1-P2A-FTH1-PGK-eGFP-BleoR and pzDONOR-CAG-DMT-1-PGK-eGFP-BleoR plasmids were used as template in positive control PCR reactions, whereas water and DNA extracted from wild type HEK cells were used as negative controls.

Western blotting

Cultured cells were washed twice in PBS and lysed in RIPA lysis buffer supplemented with protease inhibitors through gentle trituration through a 23-gauge needle. Lysates were centrifuged at 20,000 g and supernatants were collected and quantified for protein concentration using the Bradford assay. Proteins were resolved by SDS-PAGE and blotted onto PVDF membranes. Membranes were blocked with 5% skim milk in TBS-T (0.05%) for 1 hour at room temperature (RT), and incubated overnight at 4 °C with the following primary antibodies at 1:1000 dilution: anti-ferritin (Abcam, ab75973); anti-DMT-1 (Abcam, ab55735); anti-2A peptide (Novus Biologicals, NBP2-59627); alpha-tubulin (Abcam, ab2144); and anti-HA (Sigma Aldrich, #11867423001). The next day, membranes were washed 5 x 5 min in TBS-T and then incubated for 1 hour at RT in HRP-conjugated secondary antibody. Chemiluminescent signals were visualized with a Bio-Rad ChemiDoc^{TM}.

Transmission electron microscopy (TEM)

Cells were examined with transmission electron microscopy (TEM) for confirmation of nanoparticle formation and subcellular localization, as described in previous reports for tracking exogenous nanoparticles (Schrand et al., 2010). Cells were cultured with 0.2mM manganese chloride (MnCl$_2$) for 24 hours before harvesting. Cells were washed three times with complete media for 10-minute durations at

37°C to remove excess Mn. Cells were gently centrifuged for 5 minutes at 300g and re-suspended to remove residual Mn or aggregates before fixation. Primary fixation was carried out in 1% glutaraldehyde and 4% formaldehyde in 0.1M phosphate buffer (pH7.2) for 1 hour at RT. The fixative solution was then replaced, and the sample was left at 4°C overnight. Cells were then washed three times for 30-minute durations with 0.1M phosphate buffer at RT before secondary fixation. Samples were post-fixed with 1% osmium tetroxide in phosphate buffer for 1 hour at RT in the dark and then washed three times in 30-minute durations. Samples were then dehydrated by serial immersion in ethanol solutions of 30, 50, 80 and 95% for 20-minute intervals until 100% for 45 minutes at RT. A final wash with propylene oxide was conducted twice for 15-minute durations. The samples were then infiltrated with epoxy resin using a graded series of epoxy-propylene oxide before solidification with heat (60°C) for 48 hours. Thin sections of 90-100nm were then cut and stained with uranyl acetate and Reynold's lead citrate before imaging on a FEI Talos L120C TEM system with an accelerating voltage of 80kV at the Faculty of Medicine, University of Toronto (Toronto, Canada). TEM imaging was also conducted on purified ferritin extracts from cells labeled with Mn as described above. After washing and harvesting cells, intact ferritin particles were extracted and purified by a gentle immunoprecipitation protocol modified to preserve complexed ferritin nanoparticles. In brief, collected cells were lysed with mild lysis buffer (50mM Tris-HCl pH 7-8.5, 150 mM NaCl, 1% NP-40, 0.1% sodium deoxycholate, and 10% protease inhibitor) with physical trituration through a 23-gauge needle. Lysates were then spun down at 20,000 g for 10 minutes at 4°C. The remaining pellets were incubated with 1ug of anti-ferritin antibody (ab75973) overnight at 4°C with rocking. Following antibody binding, protein A/G beads were added for 4 hours with rotation. Beads were then collected by centrifugation and washed 3 times in the aforementioned lysis buffer with the addition of 0.1% bovine serum albumin (Bioshop, ALB001). Purified ferritin protein was then eluted with 200mM Glycine-HCl pH 3 at RT and then neutralized with 1M Tris-HCl, pH 9.5. Purified ferritin extracts were then immediately deposited on carbon-film coated grids (CF300-Cu, Electron Microscopy Sciences) that were glow discharged with a PELCOeasiGlow™. Grids were then washed three times with ultrapure

water. Grids were dried by solvent wicking and imaged on a FEI Talos L120C TEM with an accelerating voltage of 120kV at the Faculty of Medicine, University of Toronto (Toronto, Canada).

Inductively coupled plasma atomic emission spectroscopy (ICP-AES)

Manganese presence and content was determined analytically by inductively coupled plasma atomic emission spectroscopy (ICP-AES). Purified ferritin extracted from Mn-labeled cells as previously described was digested with concentrated nitric acid (HNO_3) with TraceSELECT (Fluka Analytical) at 50°C with sonication for 7 hours (Haedicke et al., 2016). Samples were then diluted to 2% w/v HNO_3 before analysis on an Optima 7300 DV ICP-AES spectrometer at the Department of Chemistry, University of Toronto (Toronto, Canada).

Cellular toxicity analysis

To investigate the potential toxicity from overexpressing ferritin or DMT-1, or from iron and manganese supplementation, we assessed metabolic activity, proliferation, and viability of all cells. The WST-1 assay utilizes an UV convertible salt that is activated by cellular esterases. The degree of activation quantitatively measures the rate of enzymatic activity in metabolically viable cells which provides an indication of cell proliferation and metabolic rate. All cells were seeded at an initial density of 2000 cells per well of a 96-well plate and then cultured for 96 hours so that the assay would emphasize any impact on cell proliferation. After 24 hours from plating, cells were dosed with Mn (0.2mM) for 24 hours or iron (0.9mM) for 72 hours (the optimal labeling conditions required for MR contrast). All cells were washed after supplementation. Prior to imaging, culture medium was removed from each well and replaced with fresh medium containing WST-1 reagent (1:10 dilution) for 1 hour before measuring absorbance at 450 nm with a PerkinElmer Envision 2104 Multilabel Plate Reader (MA, USA).

Cell viability was further assessed by the live/dead viability/cytotoxicity kit for mammalian cells (Molecular Probes, Invitrogen), whereby live cells are stained fluorescent 'green' with a cell permeable/enzymatically activatable dye (Calcein AM, Ex/Em: 494/517nm) and dead cells are stained

'red' by a cell impermeable/DNA binding dye (Ethidium homodimer-1, Ex/Em: 528/617nm). A third cell permeable/DNA binding dye (Hoescht 33342, Ex/Em: 345/460nm, Sigma Aldrich) was utilized for nucleus staining to aid cell counting measurements. All cells were seeded at an initial density of 20,000 cells per well of a 24 well plate and then cultured for 96 hours. After 24 hours from plating, cells were dosed with Mn (0.2mM) for 24 hours and iron (0.9mM) for 72 hours, same as above. All cells were washed after supplementation. Prior to imaging cells were incubated with 2 μM Calcein AM live stain, 4 μM EthD-1 dead stain, and 1ug/ml Hoescht nuclear stain in PBS (1×; pH 7.4) with calcium and magnesium for 45 min at 37°C. Imaging was performed on a Leica DMi8 inverted epifluorescence microscope using a green fluorescent protein (GFP), Texas Red (TXR) and DAPI filter cube to visualize the live, dead, and nuclear stain, respectively.

In-vitro cellular MRI

To assess the capability of each reporter gene for MRI contrast generation, cells were dosed with free iron (ferric ammonium citrate) or manganese before live cell imaging with MRI. Ferritin-overexpressing cells were dosed with either Mn $(0 - 0.2\text{mM})$ or iron $(0 - 0.9\text{mM})$ for 24, 48, or 72 hours until significant contrast was observed. DMT-1-overexpressing cells were dosed with Mn $(0 - 0.9\text{mM})$ for 1 hour. Labeling concentrations and times were chosen based upon standard doses used in live animal imaging and previous reports (Bartelle et al., 2013; Iordanova et al., 2010). After dosing, cells were washed with complete media three times to remove excess supplement and then trypsinized, pelleted, and washed again. Washed cells were then transferred into 115x4m Wintrobe sedimentation tubes (Kimble CHASE, Vinelad, NJ) and centrifuged gently at 300g for 5 minutes. Complete media was added without disturbing the pellet. The cells were then taken immediately on ice to the MRI scanner. Cell pellets were loaded into a custom-made ULTEM$^{\text{TM}}$ resin holder and imaged in a 32-channel head coil on a clinical 3T MR scanner (Achieva TX, Philips Medical Systems) at the Hospital for Sick Children (Toronto, Canada). High resolution T$_1$-weighted images were acquired using a two-dimensional (2D) spin-echo (SE) sequence: repetition time (TR) = 100 ms, echo time (TE) = 14.1 ms, 60 mm field-of-view (FOV), 2 mm slice

thickness, 0.5 mm × 0.5 mm in-plane resolution, and number of signal averages (NSA) = 8. T_1 mapping was performed using inversion recovery turbo SE: TR = 3000 ms, TE = 18.5 ms, 60 mm FOV, 2 mm slices, 0.5 × 0.5 mm in-plane resolution, and inversion time (TI) = (50, 100, 250, 500, 750, 1000, 1250, 1500, 2000, and 2500) ms. After image acquisition, the data were analyzed on a 2 mm deep cylindrical volume within each cell pellet. T_1 values were calculated on a pixel-by-pixel basis using in-house software developed in Matlab (v. 8.1) (Cheng and Wright, 2006). Quantitative T_2 relaxation times were measured using a 2D multiecho SE sequence: TR = 2000 ms, 32 echoes with minimum TE = 7.6 ms and 7.6 ms echo spacing, 60 mm FOV, 2 mm slice thickness, and 0.5 mm × 0.5 mm in-plane resolution.

In-vivo cell-tracking with MRI

This study was approved by the Lab Animal Services of the Hospital for Sick Children (protocol #36770), and all procedures were conducted in accordance with the Canadian Council on Animal Care. Five-week old female NOD/SCID mice (N = 10, Charles River Laboratories) weighing 22-25g, were injected with $3x10^6$ cells in serum-free media intramuscularly in each inner leg. Nine experimental animals had cell reporter lines (bright-ferritin, dark-ferritin, and DMT-1, N = 3 per line) and wild type cells injected I.M. in contralateral legs and imaged. One control animal (N = 1) was injected with ferritin- and DMT-1-overexpressing cells in contralateral legs and supplemented with saline. The bright-ferritin and DMT-1 experimental groups were injected with 0.4mmol/kg $MnCl_2$ subcutaneously on the dorsum 24 hours after cell injection. MRI imaging was conducted on Day 1 (pre-contrast prior to $MnCl_2$ injection) and Day 2, 4, 5, and 7. One DMT-1 animal was injected twice with $MnCl_2$ subcutaneously at 24- and 96-hours post-cell injection to test the recovery of bright contrast. The dark-ferritin experimental group did not receive any supplement for the first 48 hours to assess the ability of ferritin to produce contrast from endogenous iron sources. Afterward 48 hours, each mouse was orally supplemented with 2 mmol/kg of iron (ferric ammonium citrate) once daily. One of the three mice died during oral gavage. These mice were imaged on Day 1, 2, 5, and 7 to observe pre-contrast signal, endogenously induced contrast, and supplement-induced contrast. Following day 7, all mice were sacrificed, and inner leg muscles were harvested and fixed with

4% paraformaldehyde. Fixed tissues were then embedded in paraffin and prepared as 5μm sections before mounting on glass slides. After de-paraffination, sections were stained with hematoxylin and eosin (H&E) and assessed for the presence of morphologically distinct HEK cells distributed within leg skeletal muscle (Fig. S2).

MRI imaging was conducted on mice placed in a prone position inside an 8-channel wrist coil on a clinical 3T MR scanner (Achieva TX, Philips Medical Systems). Mice were induced on 5% isoflurane and maintained on 2% isoflurane (Forene, Abbott Labs, Baar, Switzerland) in pure oxygen (2 L/min flow rate). Body temperature was maintained by placing under the animal a water blanket (HTP-1500, Adroit Medical Systems, London, TN) set at 41°C. Mice were imaged using two T_1-weighted sequences: (1) 2D SE sequence with fat saturation with TR=507ms, TE=17.6ms, NSA=2, FA=90°, FOV=100mm, 1 mm slice thickness, and 0.3 mm x 0.3 mm in-plane resolution, and (2) non-fat saturated 3D fast field gradient echo (FFE) sequence with TR=10.07ms, TE=5.21ms, NSA=3, FA=30°, FOV=100mm, and similar resolutions as the 2D SE. Quantitative T_1-mapping was performed using a variable flip-angle method (Cheng and Wright, 2006). To capture T_2- and T_2^*-weighted contrast, a T_2-weighted 2D turbo SE sequence with TR=3000ms, TE=50ms, NSA=3, FA=90°, and echo train length (ETL)=8, and a T_2^*-weighted 2D FFE with TR=500ms, TE=20ms, NSA=3, FA=20° and echo train length of 1 was used, respectively. Quantitative T_2 and T_2^*- mapping was performed using a 2D multi-shot turbo SE sequence with ETL=6, minimum TE=13ms, TR=2000ms, and a 2D multi-shot FFE with ETL=32, minimum TE=4.4ms, TR=99.6ms, and FA=20°, respectively.

Statistical analysis

Descriptive statistics and data plotted are represented as mean ± SEM, except for in-vitro and in-vivo T_1/T_2 and R_1/R_2 values, which are shown as mean ± SD. All immunoblots shown are representative blots from a minimum of three independent replicates. Normally distributed data were analyzed using a two-

way analysis of variance (ANOVA) followed by a Tukey-Kramer test for post-hoc analysis. Significance is reported at a p-value of 5%.

SUPPLEMENTAL REFERENCES

Bartelle, B.B., Szulc, K.U., Suero-Abreu, G.A., Rodriguez, J.J., and Turnbull, D.H. (2013). Divalent metal transporter, DMT1: a novel MRI reporter protein. Magnetic Resonance in Medicine *70*, 842-850.

Cheng, H.L., and Wright, G.A. (2006). Rapid high-resolution T(1) mapping by variable flip angles: accurate and precise measurements in the presence of radiofrequency field inhomogeneity. Magnetic Resonance in Medicine *55*, 566-574.

Haedicke, I.E., Li, T., Zhu, Y.L.K., Martinez, F., Hamilton, A.M., Murrell, D.H., Nofiele, J.T., Cheng, H.M., Scholl, T.J., Foster, P.J.*, et al.* (2016). An enzyme-activatable and cell-permeable Mn(III)-porphyrin as a highly efficient T1 MRI contrast agent for cell labeling. Chem Sci *7*, 4308-4317.

Iordanova, B., Robison, C.S., and Ahrens, E.T. (2010). Design and characterization of a chimeric ferritin with enhanced iron loading and transverse nmr relaxation rate. Journal of Biological Inorganic Chemistry *15*, 957-965.

Lam-Yuk-Tseung, S., and Gros, P. (2006). Distinct targeting and recycling properties of two isoforms of the iron transporter DMT1 (NRAMP2, Slc11A2). Biochemistry *45*, 2294-2301.

Lee, S.H., Hadipour-Lakmehsari, S., Murthy, H.R., Gibb, N., Miyake, T., Teng, A.C.T., Cosme, J., Yu, J.C., Moon, M., Lim, S.*, et al.* (2020). REEP5 depletion causes sarco-endoplasmic reticulum vacuolization and cardiac functional defects. Nat Commun *11*, 965.

Schrand, A.M., Schlager, J.J., Dai, L., and Hussain, S.M. (2010). Preparation of cells for assessing ultrastructural localization of nanoparticles with transmission electron microscopy. Nat Protoc *5*, 744-757.